High-Frequency, High-Temperature Fretting Experiments

J. F. Matlik [a,1], T. N. Farris [b], F.K. Haake [c], G. R. Swanson [d], and G. C. Duke [e]

[a] *Rolls Royce Corporation, Box 420, Indianapolis, IN, 46206-0420, USA*

[b] *School of Aeronautics and Astronautics, Purdue University, 315 North Grant Street, West Lafayette, IN, 47907-2023, USA*

[c] *United Technologies Corporation, Pratt and Whitney Space Propulsion, 17900 Beeline Hwy, Jupiter, FL 33478*

[d] *EM20, Damage Tolerance Assessment Branch, NASA, Marshall Space Flight Center, AL 35812*

[e] *Sverdrup Technology, Inc., MSFC Group, 6703 Odyssey Drive, Suite 303, Huntsville, AL 35806*

Abstract

Fretting is a structural damage mechanism observed when two nominally clamped surfaces are subjected to an oscillatory loading. A critical location for fretting induced damage has been identified at the blade/disk and blade/damper interfaces of gas turbine engine turbomachinery and space propulsion components. The high-temperature, high-frequency loading environment seen by these components lead to severe stress gradients at the edge-of-contact. These contact stresses drive crack nucleation and propagation in fretting and are very sensitive to the geometry of the contacting bodies, the contact loads, materials, temperature, and contact surface tribology (friction). To diagnose the threat that small and relatively undetectable fretting cracks pose to damage tolerance and structural integrity of in-service components, the objective of this work is to develop a well-characterized experimental fretting rig capable of investigating fretting behavior of advanced aerospace alloys subjected to load and temperature conditions representative of such turbomachinery components.

Key words: fretting, fretting fatigue, high frequency, contact

[1] This work was carried out at Purdue University. Funding was provided in part by a National Science Foundation fellowship for J.F. Matlik and in part by Pratt and Whitney Space Propulsion under subcontract with the National Aeronautics and

Fretting is an aggressive combination of wear, corrosion, and fatigue associated with small-scale relative sliding that arises in nominally clamped structural components that undergo an oscillatory or vibratory loading. The associated edge-of-contact stresses sometimes initiate and grow cracks in a phenomenon known as fretting fatigue. Fretting contact is unique from sliding contact in that the tangential load producing the relative oscillatory motion is less than that required to produce gross sliding over the whole of the contact surface. This leads to a small central patch of no relative motion within the two contacting surfaces called the *stick* zone and is flanked by regions of sliding or relative motion termed the *slip* zone. In general, the relative slip amplitude associated with this condition of *partial slip* is on the order of 25 - 100 microns. The relative motion within the slip zone of the contact results in wear and then subsequent corrosion and fatigue of the subsurface material.

Systems that have seen fretting damage include but are not limited to helicopters, fixed-wing aircraft, trains, ships, automobiles, farm machinery, engines, construction equipment, orthopaedic implants, artificial hearts, rocket motor cases, electrical wires and wire rope to name a few [1]. Hills and Mugadu have provided an overview of the progress current researchers have had in studying the fretting problem [2] and Farris, Murthy and Matlik have addressed the issue of fretting fatigue with regard to structural integrity of mechanical systems [3].

A critical location for fretting induced damage has been identified at the blade/disk and blade/damper interfaces of gas turbine engine turbomachinery and space propulsion components. The goal of the following effort is to develop a well-characterized experimental setup to investigate the fretting behavior of advanced materials employed in these turbine engine components in service today. Ultimately, it is hoped that the following work will aid in development of component life prediction schemes and design metrics used to manage and minimize performance degradation of such components due to fretting damage mechanisms.

Due to the plethora of mechanical, physical, and environmental factors contributing to the fretting phenomenon and with the ever present cloud of ambiguity permeating the definitions of fretting crack nucleation and propagation, fretting research demands well defined, well controlled experimental investigations to explicate factor effects which still remain a mystery. The majority of this work will be aimed at specifically mimicing the load and temperature conditions as seen by high performance turbomachinery. To this end, a comprehensive review of fretting experimentation will not be presented here. For the interested reader, an excellent review of fretting fatigue historically

Space Administration (NASA) managed by Greg Swanson of the Marshall Space Flight Center (MSFC).

was provided by Waterhouse [4] with further details about the underlying mechanics of fretting fatigue having been reviewed by Szolwinski and Farris [5] and Hills and Nowell [6]. To experimentally investigate the fretting behavior of advanced materials, a well-characterized, high-frequency, high-temperature fretting experimental rig has been designed and constructed. The details of the designed rig, calibration and experimental methods used in realizing this goal will now be presented.

1 Fretting Rig

Any fretting experimental setup must be capable of applying and monitoring the clamping load normal to the contact, P, and oscillatory tangential load history, Q, that leads to the development of fretting cracks. The desired condition of partial slip must then be sustained during testing by applying a tangential load less than the coefficient of friction, μ, times the normal load ($|Q| < \mu P$). Earlier work has detailed the design of a high frequency fretting rig that employed the use of a piezoelectric stack actuator to generate the tangential loading, Q, at the contact [7]. This enabled the desired order of magnitude increase in loading frequency as compared to fretting fixtures used in standard servo-hydraulic fatigue machines [8,9]. The current rig was constructed by modification of the fretting fixture and main load train of the piezoelectric rig presented by Matlik and Farris (2003).

1.1 Design of the Contact

For meaningful analysis and determination of critical parameters associated with fretting contact, it is mandatory that a clear understanding of contact tractions and stresses be monitored continuously throughout the experiment. This requires a contact design scheme that allows for experimentally measured loads remote to the contact to be resolved to contact tractions and stresses via an appropriate analysis scheme. To allow for a rigorous analysis of contact pressure, shear traction distribution, and interior stress fields, the previous designs have adopted a fretting contact geometry similar to that originally devised by Bramhall and O'Connor [10,11] and implemented by Hills and Nowell [8]. In order to observe crack nucleation due solely to the presence of contact fretting loads, the specimen design was altered to remove the bulk stress loading inherent to fretting fatigue loading of dog-bone specimen geometries as investigated by previous researchers [8,9,7]. The chosen specimen geometry can be seen in Figure 1. Each specimen has a mating contact pad. The pad geometry choice allows for many variations in contact geometry to be investigated. Pad geometry can be machined to cylindrical profiles [8],

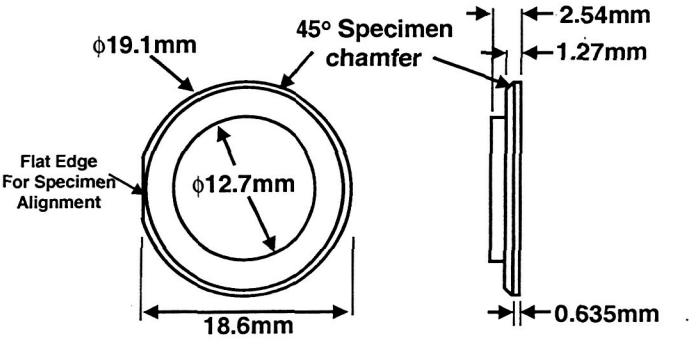

Fig. 1. Geometry of single crystal fretting specimen.

spherical profiles [12], or any variation of a nominally flat pad with rounded edges [13]. For this work, the pad geometry was chosen to be spherical to avoid free-edge effects, localize fretting damage, and to mimic the classical 3D Hertzian contact configuration. The chosen pad geometry can be seen in Figure 2.

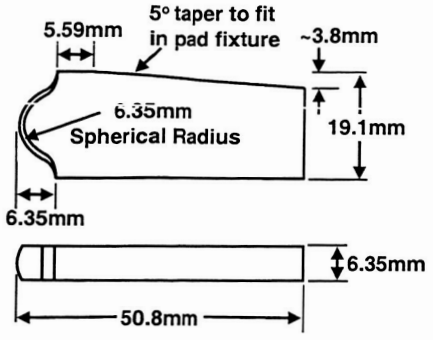

Fig. 2. Geometry of fretting pad.

1.2 Superstructure

The designed high-temperature, high-frequency fretting rig was constructed and mounted on a custom built machine base. Figure 3 shows a picture and schematic of the rig. Standard vibration dampening feet were used to minimize

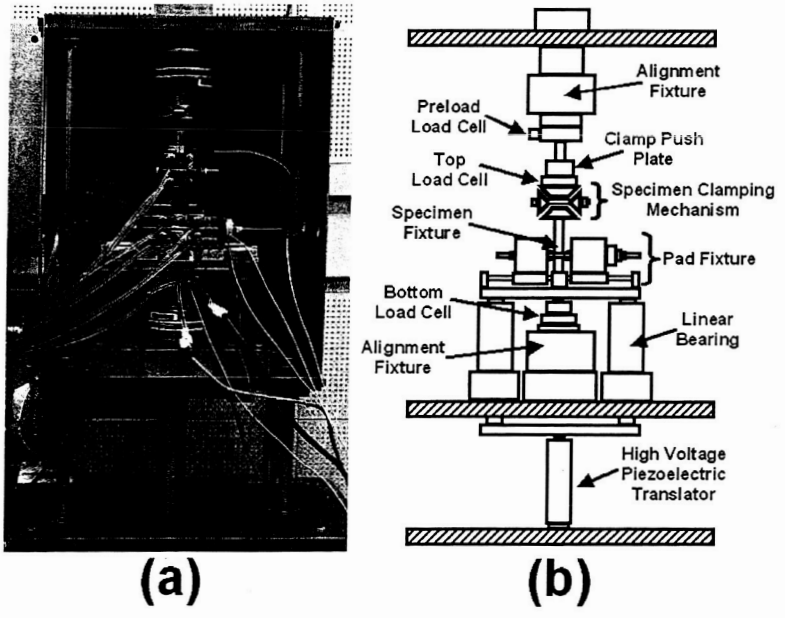

Fig. 3. (a) Picture and (b) schematic of the high-temperature, high-frequency fretting load frame

vibrational response of the rig during high frequency operation. The machine

base also served as a house for the high voltage amplifier used to power the piezoelectric actuator. The fretting test fixture and load train were built between three 25 mm (1 inch) thick hot rolled steel base plates each separated by four 25 mm diameter, solid, chrome plated, 440C Stainless Steel shafts (see Figure 3). The overall height of the rig is approximately 1.83 m (6 feet) from the ground to the top base plate. The 610x356x25 mm (24x14x1 inch) base plate of the rig was bolted to the 762x610x25 mm (30x24x1 inch) Mattison ground stainless steel top of the machine base. The middle base plate serves as an anchor for the bottom of the load train and a support plate to maintain alignment of the linear bearings used in tangential load transfer from the piezoelectric actuator to the contact surface. To increase overall rig rigidity and therefore increase the applied tangential load, a set of thin 3.2 mm (1/8 in) thick metal plates were fastened to the outside of the top and middle base plates.

1.3 Specimen Fixture

Since the single crystal properties of the specimen are dependent on the loading direction, the specimen geometry includes a flat edge which is used to identify the desired specimen orientation. To maintain consistency, the flat recess was machined such that it would always be at the left when mounting in the specimen fixture. Two specimen conforming slots were machined into opposite sides of the specimen fixture. Each specimen is clamped in the specimen fixture for testing as illustrated in Figure 4. The top specimen fixture is slid up for specimen placement. After properly orienting each of the top-hat specimens in their conforming slots, the top fixture is slid down to clamp the specimens in place. The outer rim of the specimen geometry has a 45^o chamfer to aid in specimen clamping. The specimen clamping mechanism (as seen in Figure 3) is used to apply a clamping load to secure each specimen in position. Load cells located above and below the specimen fixture are used to specify a desired clamping load as well as monitor the applied tangential load during the course of the experiment.

1.4 Temperature Elevation

The contact region is heated via radiant (and convection with air) heating of the contact region using Norton Crystar (SiC) igniters (Model #:271, type N mounting configuration). A photograph and schematic of the igniter placement with respect to the pad and specimen fixtures can be seen in Figure 5 and Figure 6, respectively. The igniters are driven by an OMEGA CSC32 benchtop temperature meter and controller. The temperature for the PID control is

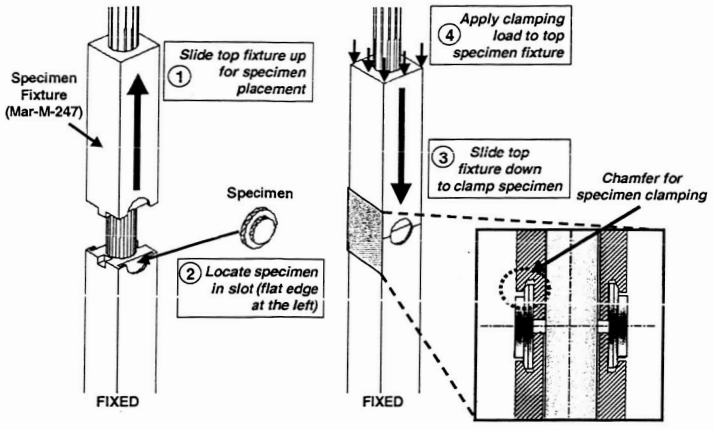

Fig. 4. A schematic of the specimen fixture highlighting the specimen clamping procedure.

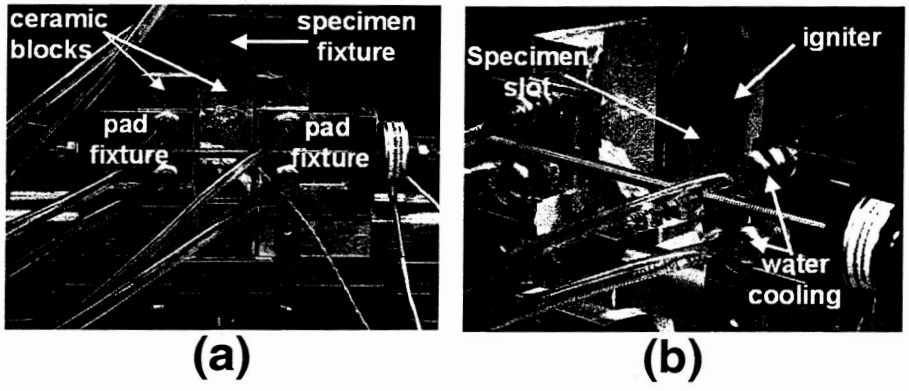

Fig. 5. (a) Picture of the high-temperature, high-frequency fretting fixture, and (b) a side view picture of the fretting rig highlighting internal fixture features and igniters for elevated temperature operation.

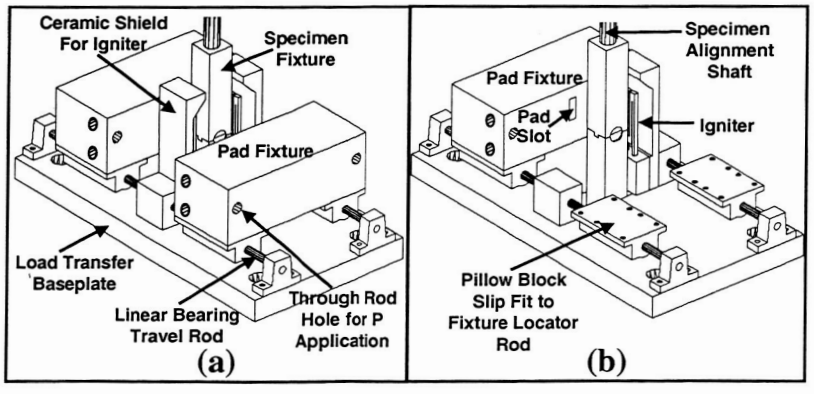

Fig. 6. (a) Schematic of the high-temperature, high-frequency fretting fixture, and (b) a partial schematic highlighting internal fixture features and igniters for elevated temperature operation.

measured using a K*type* thermocouple spot-welded to the specimen close to the contact. By covering the front face of the pad and specimen fixtures with ceramic paper, the pad fixtures and ceramic shield create the oven required for local heating of the contact to a target temperature of 649^oC. In order to accommodate the elevated temperature, the pad fixture was constructed from a titanium alloy (Ti-6Al-4V) and the specimen fixture was constructed from a high temperature nickel alloy used in turbine engines (Mar-M-247).

1.5 Pad Fixture

After clamping the specimens, each specimen has a mating contact pad (Figure 2) which is slid into the pad slot until the 5^o taper of the pad wedges against the 5^o taper of the slot in the pad fixture. The pads are then brought into contact with its mating specimen by tightening through rod nuts on the normal load transfer through rod of Figure 7. This applied normal load securely wedges the pads into place. Load washers are used on each through rod to monitor the applied normal load and minimize the potential moment that could arise from uneven tightening of the loading nuts. A set of static calibration tests were conducted to find the contact normal load transfer ratio. The load transfer ratio was consistently found to be between 98% and 99% as found by comparing the remotely measured load obtained by the load washers of Figure 7 with the load obtained by a load cell placed between the two pad fixtures.

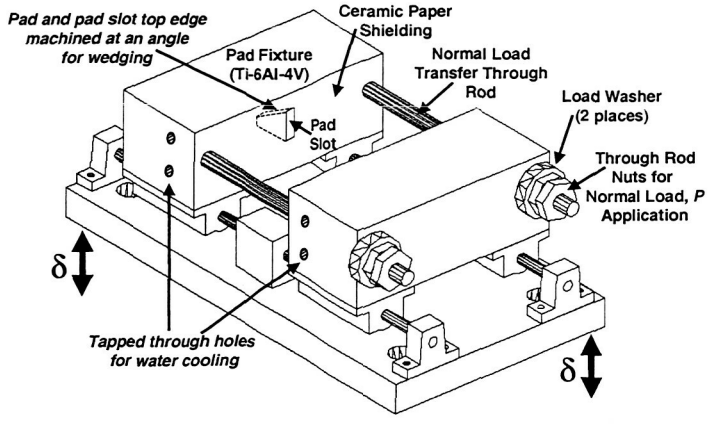

Fig. 7. A schematic of the pad fixture highlighting the load washers and nuts used to monitor and apply the normal contact load, P.

The pad fixture rides on a linear bearing travel rod providing little resistance to the applied normal load (P) while simultaneously providing significant stiffness in the tangential direction equal to the bending stiffness of the rails upon which it rides. The four brass pillow blocks machined to a slip fit with the linear bearing travel rods are also each fitted with a brass tipped set screw to

remove any clearance between the pillow block and the rod that could lead to pad fixture rocking during operation. A pair of tapped through holes exist in each pad fixture to allow for water cooling when operating at elevated temperature.

1.6 Tangential Load Application

After clamping the specimens in the specimen fixture and applying the desired normal load, the piezoelectric actuator is then engaged to displace the entire pad fixture and generate a tangential load between each pad and specimen contact pair. As seen in Figure 7, the tangential load is applied by tangential displacement, δ, of the fretting pads after contact has been established via normal loading. This tangential displacement was achieved via the use of a custom built piezoelectric stack actuator and associated amplifier.

1.6.1 Piezoelectric Stack Actuation

The piezoelectric stack-actuator chosen for the high-frequency rig was a custom built thermally stabilized piezoelectric stack-actuator (derivative of the model PSt 1000/25/200 offered by Piezomechanik GmbH). The casing of the actuator was constructed of copper which demonstrates good heat conduction characteristics. In addition, a high pre-load of 10 kilo Newtons (2250 lbs) to allow for safe symmetric operation. Unloaded operation of the piezoelectric stack showed a measured maximum displacement of 220 μm using a capacitance probe. A summary of the chosen piezoelectric stack-actuator capabilities and characteristics can be seen in Table 1.

Table 1
Piezoelectric stack actuator capabilities and specifications.

Parameter	Value	Unit
Max. operating voltage	1000	Volts
Displacement amplitude	+/- 100 (4)	μm (inx10^{-3})
Capacitance	5	μF
Stack diameter	20 (0.79)	mm (in)
Overall length	232 (9.13)	mm (in)
Pre-load	10 (2250)	kN (lbs)

The power for the piezo-stack operation came from an complimentary Piezomechanik GmbH high power amplifier (model RCV 500/15). This specific piezo/amplifier system has the unique ability to communicate between the piezo and amplifier in order to ensure safe temperature or thermostable operation. The amplifier specifications can be seen in Table 2.

Table 2
High power amplifier capabilities and specifications.

Parameter	Value	Unit
Voltage range	50–500	Volts
Peak Current	15	Amperes
Input signal	0–10	Volts
Device Bandwidth	3000	Hz

1.6.2 Tangential Load Transfer

To apply the tangential load and maintain clearance from the load train, four L-class rods were bolted into the four outside corners of the upper load transfer base plate and then passed through the middle base plate to a lower load transfer base plate to which the piezoelectric stack actuator was attached (Figure 8).

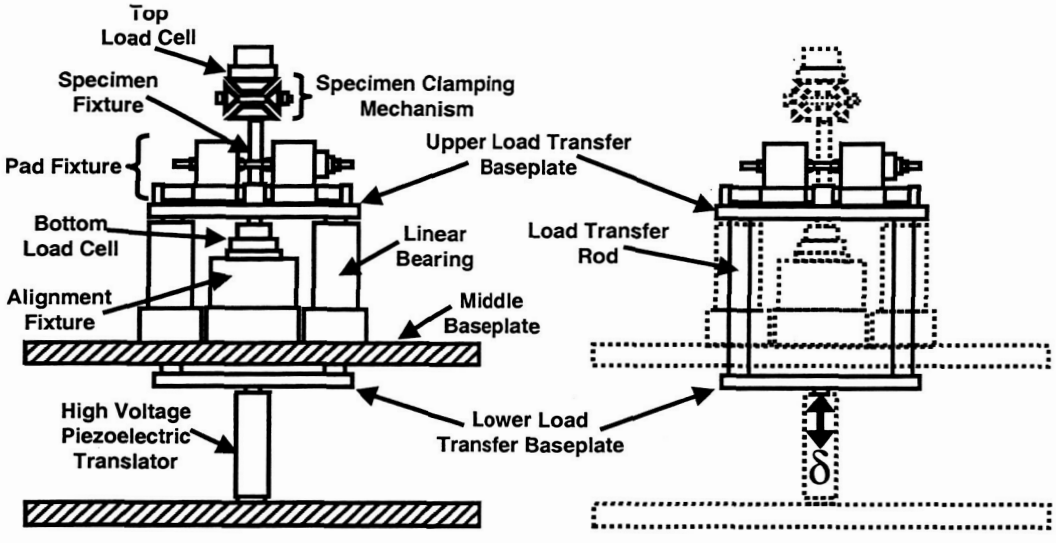

Fig. 8. A schematic illustrating the tangential load application via the piezoelectric stack actuator. Note that in the right schematic the dashed lines represent portions of the rig that are *fixed* and solid lines represent structure that is being moved by the piezoelectric stack.

The four L-class load transfer rods connected the upper and lower load transfer base plates. Four rods were chosen to ensure plate alignment during high frequency operation. The rod alignment is achieved by passing each through a flange mounted Simplicity bearing from Pacific Bearing. The Simplicity bearing is characterized by a smooth Frelon surface lining on the inside of the linear bearing. The liner wears off during operation to serve as its own lubricant and aids in dampening vibration associated with high frequency operation. The bearings prevent rotation in all axes of motion and translation in all axes except for the direction of tangential loading.

1.7 Loading Sequence

With the outlined specifics of specimen clamping, normal, and tangential load applications presented, the loading sequence of an actual fretting test will now

be summarized. A graphical illustration of the loading sequence can be seen in Figure 9.

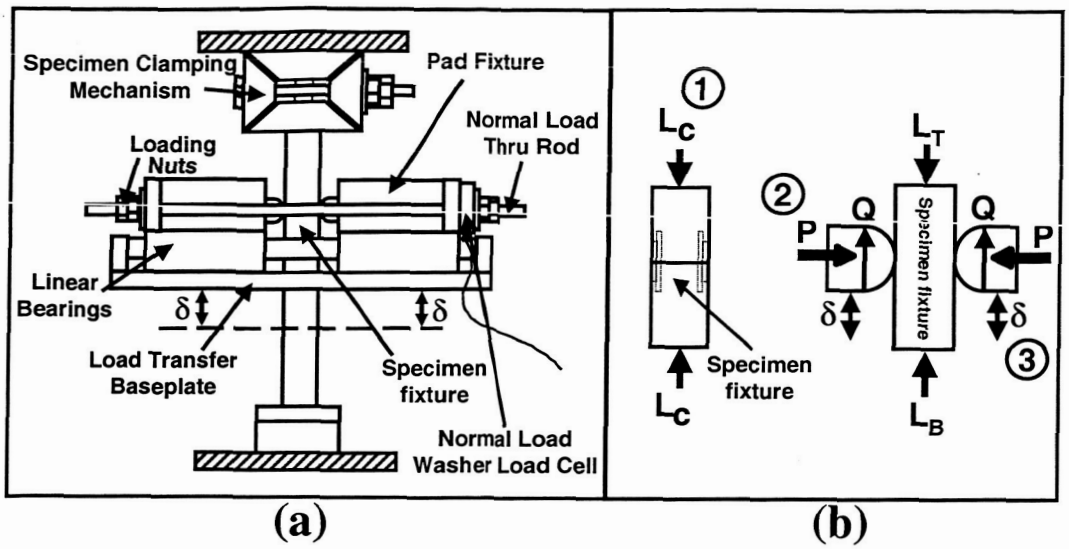

Fig. 9. (a) Schematic of the specimen and pad fretting fixture. (b) Schematic of applied loads numerically ordered as applied during experimental testing. Note that convention assumes compression to be positive.

1. Each top-hat specimen (Figure 1) is first placed in the conforming slots of the lower specimen fixture (Figure 4). The flat orientation edge machined into the left side of the specimen provides a way of dialing in the desired specimen crystal orientation. After the correct orientation is obtained, the top specimen fixture is slid down the fixture alignment rod until the specimens slide into the conforming slots on either side of the top specimen fixture. Because the fretting fixture is free to rotate about its through rod, a parallel faced alignment peace is placed between the front face of the pad fixture and the associated face of the specimen fixture to ensure that the pad/specimen clamping load applied in the next step has a load vector normal to the contact face. After rotational alignment, the specimen is secured in place by applying a clamping load via the specimen clamping mechanism seen in Figure 9. Note that at this point the pads have not been brought into contact and the measured load at the top, L_T, equals the measured load at the bottom, L_B.

2. The contact pads (Figure 2) are then slid into the pad slot so that the 5^o taper of the slot mates with that of the pad. The static normal load is then applied by tightening the set of nuts on the normal load through rod to wedge the pads in place and generate the desired contact load as measured by the external load washers (Figure 7). If operating at elevated temperature, the igniters are used to elevate the contact to the desired temperature before generation of the full contact load. As the rig heats up, thermal expansion will

cause the applied loads to fluctuate. This requires the loads to be adjusted during the heat-up process to avoid overshooting the target loads. After the rig reaches steady state at the desired operational temperature, final adjustments to the nuts on the normal load through rod are made to achieve the desired normal load value. Finally, the brass tipped set screws in the pillow blocks of the pad fixture are tightened evenly to remove any clearance that could result in poor dynamic behavior.

3. Finally, the high frequency tangential load waveform is directly applied as the piezoelectric stack actuator displaces the pads tangentially, δ, along the contact surface (Figure 9).

1.8 Simple Rig Model

In addition to measuring the initially applied specimen clamping load, the top and bottom load cells provide a way of continually monitoring the applied tangential load during testing. To better identify the mechanics of load measurement in the designed rig, a simple model can be constructed as illustrated in Figure 10. Figure 10b shows the specimen clamping loads generated by the specimen clamping mechanism. Note that in this case, the top load cell, L_T, and bottom load cell, L_B, directly measure the applied specimen clamping load, L_C, giving $L_T = L_B = L_C$. Compressive loading is taken as positive loading in this convention. Assuming the load train components can be modeled as linear springs, Figure 10c shows each component of the load train and location of the tangential load used to directly apply the cyclic fretting load desired. In this figure, k_1 represents the specimen clamping mechanism, k_2 represents the top specimen fixture, k_3 represents the bottom specimen fixture, k_4 represents the specimen locator plate(s), and the two applied forces, Q, represent the applied tangential load from each pad/specimen contact pair. Note that given the applied tangential load can be measured as $Q = 0.5(L_T - L_B)$.

Since there is no applied crack propagating bulk stress, crack propagation to fracture of the top-hat specimen is unlikely. Therefore, specimen locator plates were incorporated into the design to allow translation of the specimen fixture up the specimen alignment shaft of Figure 6b relative to the pad fixture. By replacing the fretting pads and locating a new contact location on virgin material of the specimen, the same specimen can be used for multiple fretting tests. This is done by adding or removing the locator plates (seen in Figure 10a) to shift the location of the pad contact across the specimen surface.

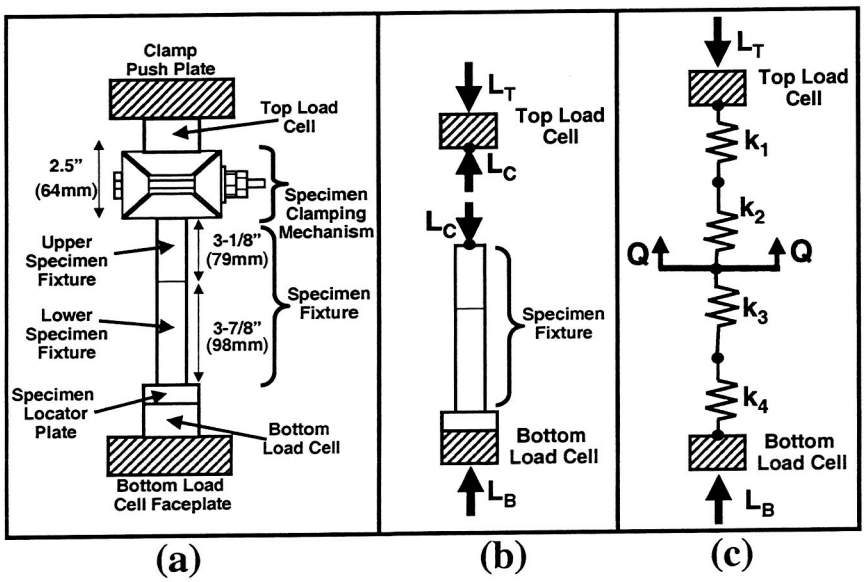

Fig. 10. A series of schematics showing (a) the load train components, (b) the forces generated for clamping the specimen in place, and (c) the load train components and loads observed in application of the tangential load, Q, through piezoelectric actuation.

2 Data Acquisition and Control Systems

For successful quantification of the fretting damage process, accurate measurement of the normal load, P, tangential load, Q, and specimen clamping load, L_c as applied by the experimental setup during the duration of the test is mandatory. The designed high frequency fretting rig monitors these fretting parameters using a series of analog sensors residing both in the fretting fixture and in the load train. The normal load is obtained by observing the calibrated output of a set of compression load washers slipped over the ends of the normal load through rods as seen in Figure 7. The tangential load and specimen clamping load can be obtained from calibrated output from the compression load cell just above the clamping mechanism, and just below the specimen locator plate as seen in Figure 10. The 100 lbs. capacity load washers used in the normal load measurement and the 1000 lbs. capacity load cells used for capturing specimen clamping and tangential loads were purchased from Omega (models LCW-100 and LCHD-1k, respectively). Each of these load measurement devices is constructed of 17-4 PH stainless steel externally with the actual load measurement occurring from foil strain gages bonded along an internal diaphragm to reduce off-center loading effects. Each has a full Wheatstone bridge circuit design. The applied load could then be determined using the measured output load cell voltage change and the load cell calibration data as obtained from the manufacturer.

The analog signal conditioning and storage of the analog output from each load cell were monitored in-situ and saved to disk for later processing through the use of a National Instruments manufactured general-purpose Signal Conditioning eXtensions for Instrumentation (SCXI) chassis (model SCXI-1000). Two of the four slots in the chassis each house a National Instruments manufactured four-channel isolation amplifier (model SCXI-1121) with excitation, isolation, and signal conditioning for the analog output from each load cell. The continuous online monitoring of each fretting fatigue experiment is achieved though LabVIEW (Laboratory Virtual Instrument Engineering Workbench), a graphical programming language that allows the user to exploit the user-friendly GUI environment by developing a series of Virtual Instruments (VIs) for interfacing and monitoring acquired data obtained from the SCXI chassis.

Control of the piezoelectric actuator is achieved by oscillating the input voltage via a Wavetek 2 MHz sweep / function generator. The Wavetek allows for variable frequency, variable R-ratio tangential loading of the contact. The magnitude of the applied tangential load varied from zero to the maximum tangential load amplitude corresponding to full-scale piezo actuator displacement. For the interested reader, further details of the data aquisition system and control systems are detailed in Matlik and Farris (2003).

3 High Frequency Calibration

Calibration of the analog sensor output was necessary to secure confidence in the contact load measurements. The calibration of the load cell output is particularly important in high frequency operation due to indeterminant frequency response characteristics of the complex system subjected to this vibration. During high frequency operation, it is first necessary to determine any critical frequency ranges in which resonant frequencies of the system interfere with accurate acquisition of data. The unique resonant behavior inherent to this experimental setup was investigated by observing the room temperature dynamic response: (1) in the direction normal to the contact as captured by the normal load cells, (2) in the direction of the applied tangential load as obtained by the load cells in the load train above and below the contact, and (3) in the out-of-plane direction as obtained by strain gages mounted to the specimen fixture in an appropriate wheatstone bridge configuration to capture out-of-plane bending strain.

The peak-to-peak input voltage (excitation) to the piezo-stack was set at a low constant value to allow a frequency sweep from 100 to 1100Hz. Input excitation was set at 1 Volt peak-to-peak. Larger excitations could potentially compromise the structural integrity of the piezo ceramic at high frequencies ($> 500Hz$) due to the dynamic loading associated with moving the mass of the pad fixture. Peaks in the ratio of load amplitude to mean load ($Load_{amp}/Load_{mean}$) as acquired in-situ by the load cell then correspond to natural frequencies of the system.

Envelopes of *safe* frequencies, ω_{safe}, can be identified by specifying an acceptable tolerance on $Load_{amp}/Load_{mean}$. This information can be used to choose rig operational frequencies away from inherent natural frequencies. After identifying safe frequency envelopes for given tolerance combinations, cycle loading waveform behavior was observed within safe frequency envelops to identify an operating frequency that gives the desired loading waveform. To get the largest possible applied tangential load, a 180^o out-of-phase L_B and L_T waveform behavior is desired since $Q = 0.5(L_B - L_T)$.

Figure 11 represents the load waveform traces as obtained at 650Hz operation. Note the dynamic response in the load cell measurements resulting in both a clean sinusoidal signal and a 180^o out-of-phase behavior between the L_B and L_T load cell measurements. This behavior results in a symmetric, sinusoidal tangential load as noted by the plot of tangential load, Q, verses captured data points in the lower right plot. Based on the frequency scan investigations and the loading waveform trace behavior, 640Hz was chosen operational frequency for the room temperature tests.

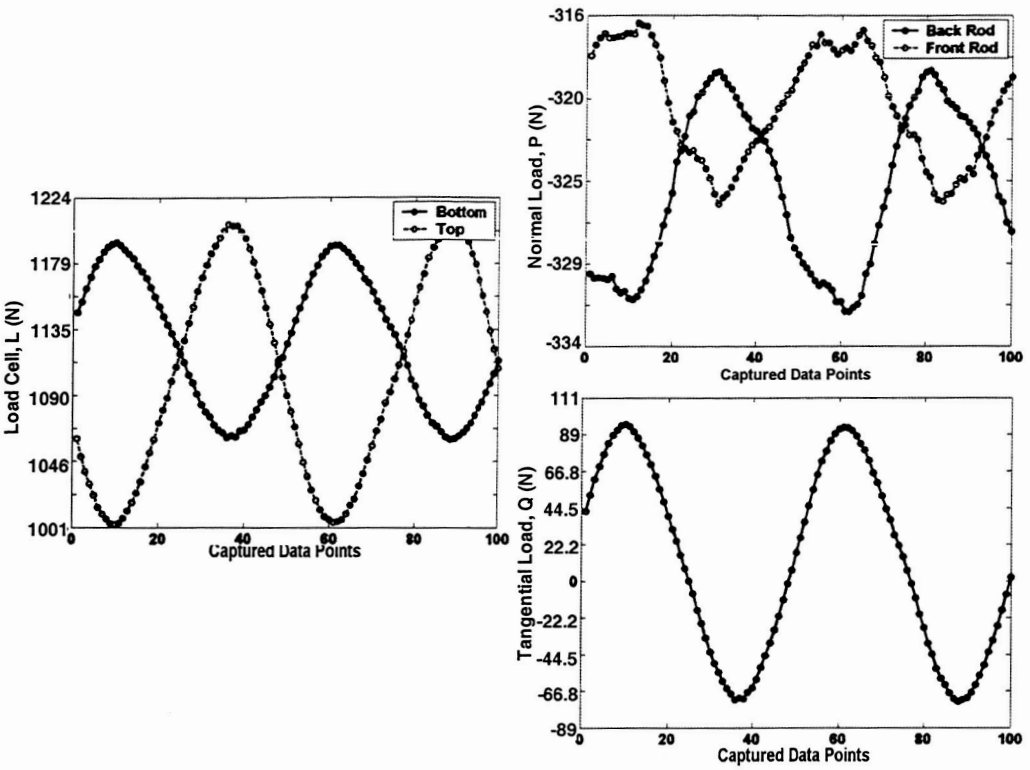

Fig. 11. Load waveforms as obtained from the experimental rig while operating at 640Hz. Note that the negative normal load (P) values indicate that the normal load washers are measuring in compression.

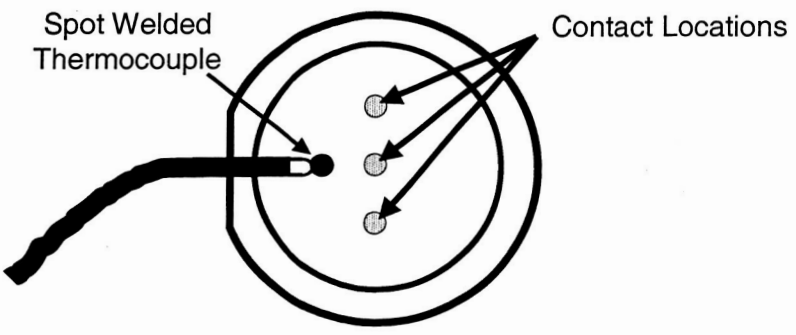

Fig. 12. Schematic identifying the location of temperature measurement by a K-type thermocouple spot welded to the specimen surface 3.2 mm to the left of the center contact. All high-temperature tests had temperature control from the thermocouple spot welded to the right specimen.

3.1 Elevated Temperature Calibration

The same dynamic calibration procedure was performed to determine changes in rig behavior during high temperature operation at 649°C (1200°F). Investigation of the frequency response and load waveform trace behavior revealed an optimum operational frequency of 650Hz. The target elevated temperature of 649°C was measured and controlled to ±1°C by a K-type thermocouple spot welded 3.2 mm to the left of the right specimen center contact as seen in Figure 12. Simultaneously monitoring thermocouple measurements of the left and right specimen temperatures revealed a maximum of ±3°C temperature variation during testing.

Preliminary high-temperature testing revealed a transient period in which heating of the rig led to an observed thermal locking between rods and honed components of the specimen fixture and pad fixture pillow blocks. As a result, it was necessary to wait approximately 30 minutes after reaching the steady state temperature of 649°C as measured by the thermocouple before starting the test. While waiting for a thermal steady state, the specimen clamping load is continually readjusted to the desired values. Finally, the contact is generated by applying a normal load and a two second run of the contact test at the safe operational frequency of 650 Hz and the desired tangential load is run as a transient shakedown of any remaining thermal lock. The loads are readjusted once again before beginning the high-temperature test.

4 Experimental Program

With the necessary experimental tools developed, it remains to develop and run a test program to experimentally investigate the mechanics of the fretting process in single crystal nickel materials. Preliminary fretting damage observations as obtained from a series of "break-in" tests are first surveyed to motivate the design of experiments that follows. The in-situ experimental loads as processed from the acquired experimental data of the testing program are then presented. Finally, an assessment of the damage resulting from the test program proceeds with a survey of the crack locations and orientations as observed on the fretted SCN specimen surface as observed through scanning electron microscopy.

5 Test Matrix Development

Previous research has shown that the fatigue and fracture behavior of SCN material differs with operating temperature [14]. For this reason, testing was chosen to be performed at room temperature (21^oC) and at elevated temperatures characteristic of high performance turbomachinery operation (538°C and 649°C). Previous research has also shown that SCN material orientation can have a significant effect on the subsurface stresses [15]. As a result, specimens were machined to orient the tangential loading direction along a crystal principal axis and at secondary orientation directions $\pm 30^o$ between principal axes.

Although the specimen orientation was unknown in preliminary testing, post-processing of the load data obtained in-situ revealed that cracking occurred in specimens with normal loads (P) greater than 556 N, tangential load amplitudes (Q_{amp}) greater than 62 N, and for total loading cycles between N=3,000,000 and N=11,000,000. To limit the number of contact variables, the target normal load was chosen to remain constant at a value comparable to that in which cracking behavior, P = 534 N. An upper tangential load magnitude magnitude of, Q_{max} = 98 N, was set by the capability of the piezostack. With cracking observed at or above Q_{amp} = 62N, target tangential loads of 98N, 80 N, 62 N, and 44 N were chosen. Finally, since total failure of the specimen does not occur, the number of fretting cycles are also specified. With fretting cracks observed under experimental fretting loads as early as N=3,000,000 cycles, testing was chosen to be performed at 1,000,000, 5,000,000, and 10,000,000 cycles. These testing goals were then used to construct the testing matrix outlined in Table 3.

Experiments labeled 'HFRT###' represent high-frequency, room-temperature ($\approx 21^oC$) tests for which the material orientation was controlled and is known. The [0 1 0] axis of the single crystal was controlled to be oriented in the z-direction according to the coordinate system defined in the finite element analysis. The orientation value, Θ, reported in Table 3 then refers to the angular degree measurement between the x'-axis and the [0 0 1] material axis as illustrated in Figure 13a. In order to save expense of specimen machining, the fretting fixture was also designed to allow shifting of the specimen relative to the contact pad in the x'-axis direction so that multiple contact tests could be run on a single specimen. Specifically, contact tests can be run on any one specimen at an x'-axis location of +3.2 mm, 0 mm, or -3.2 mm. These contact locations are reported in Table 3 and can be seen graphically in Figure 13b. Experiments labeled 'HFHT###' represent high-frequency, high-temperature (538^o and 649^oC) tests for which the material orientation was controlled and is known according to the convention mentioned previously.

Table 3
Test matrix outlining the high-frequency fretting test program. Note that all the tests had a target normal load, P, of 534 N.

Expt. ID	Left Spec. ID	Left Spec. Θ (deg)	Right Spec. ID	Right Spec. Θ (deg)	Target P (N)	Target Q_{amp} (N)	Contact Location (mm)	Target Temp. (^oC)
HFRT005	J3-30D-01	-30	J3-30D-02	30	534	62	0	21
HFRT006	J3-30D-01	-30	J3-30D-02	30	534	80	-3.2	21
HFRT007	J3-30D-01	-30	J3-30D-02	30	534	80	+3.2	21
HFRT008	J3-30D-03	30	J3-30D-04	-30	534	80	0	21
HFRT009	J3-30D-03	30	J3-30D-04	-30	534	62	-3.2	21
HFRT010	J3-30D-03	30	J3-30D-04	-30	534	62	+3.2	21
HFRT011	J3-001-05	0	J3-001-06	0	534	80	0	21
HFRT012	J3-001-05	0	J3-001-06	0	534	80	-3.2	21
HFRT013	J3-001-05	0	J3-001-06	0	534	80	+3.2	21
HFRT014	J3-001-07	0	J3-001-08	0	534	62	0	21
HFRT015	J3-001-07	0	J3-001-08	0	534	62	-3.2	21
HFRT016	J3-001-07	0	J3-001-08	0	534	62	+3.2	21
HFHT001	J3-001-13	0	J3-001-14	0	534	80	0	538
HFHT002	J3-001-13	0	J3-001-14	0	534	80	-3.2	538
HFHT003	J3-001-13	0	J3-001-14	0	534	80	+3.2	538
HFHT004	J3-30D-05	??	J3-30D-06	??	534	80	0	538
HFHT005	J3-30D-05	??	J3-30D-06	??	534	80	-3.2	538
HFHT006	J3-30D-05	??	J3-30D-06	??	534	80	+3.2	538
HFHT007	J3-001-15	0	J3-001-16	0	534	80	0	649
HFHT008	J3-001-15	0	J3-001-16	0	534	80	-3.2	649
HFHT009	J3-001-15	0	J3-001-16	0	534	80	+3.2	649
HFHT010	J3-30D-07	??	J3-30D-08	??	534	80	0	649
HFHT011	J3-30D-07	??	J3-30D-08	??	534	80	-3.2	649
HFHT012	J3-30D-07	??	J3-30D-08	??	534	80	+3.2	649
HFHT014	J3-30D-09	??	J3-30D-10	??	534	98	-3.2	649
HFHT015	J3-30D-09	??	J3-30D-10	??	534	98	+3.2	649
HFHT016	J3-001-17	0	J3-001-18	0	534	98	0	649
HFHT018	J3-001-17	0	J3-001-18	0	534	98	+3.2	649
HFHT019	J3-001-19	0	J3-001-20	0	534	62	0	649
HFHT020	J3-001-19	0	J3-001-20	0	534	62	-3.2	649
HFHT021	J3-001-19	0	J3-001-20	0	534	62	+3.2	649
HFHT022	J3-30D-11	??	J3-30D-12	??	534	62	0	649
HFHT023	J3-30D-11	??	J3-30D-12	??	534	62	-3.2	649
HFHT024	J3-30D-11	??	J3-30D-12	??	534	62	+3.2	649
HFHT025	J3-001-21	0	J3-001-22	0	534	98	0	649
HFHT026	J3-30D-13	??	J3-30D-14	??	534	98	0	649

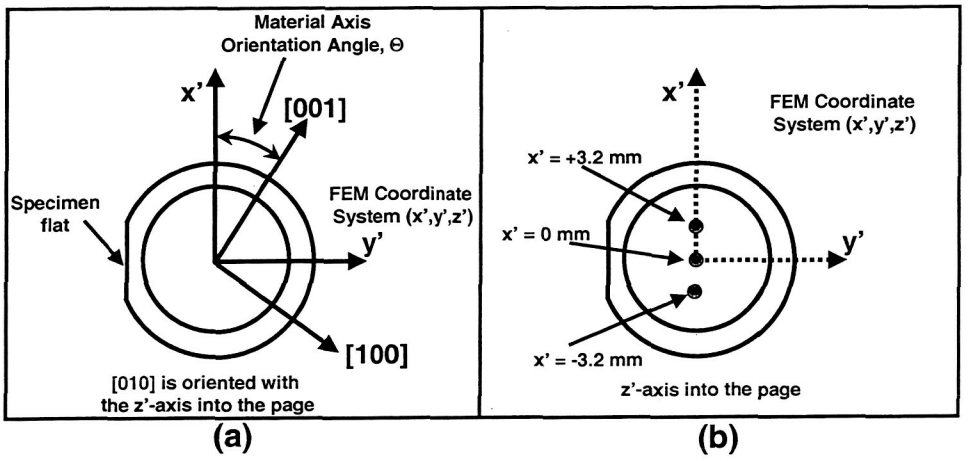

Fig. 13. (a) Schematic highlighting material orientation with respect to finite element defined coordinate system via the orientation angle, Θ. (b) Schematic highlighting the three possible contact locations along the x'-axis.

Table 4
Experimental conditions for high frequency fretting fatigue tests of SCN on Inconel at room and elevated temperatures.

Expt. ID	P_{mean} (N)	P_{amp} (N)	Q_{mean} (N)	Q_{amp} (N)	L_c (N)	Temp (^oC)	ω (Hz)	Fretting Cycles
HFRT005	556	3.78	-0.09	64.1	1032	21	640	10,000,000
HFRT006	583	4.89	-3.56	80.5	1041	21	640	10,250,000
HFRT007	569	6.67	-4.45	81.8	1090	21	640	5,000,000
HFRT008	525	6.23	-3.11	81.0	1036	21	640	1,000,000
HFRT009	552	5.78	0.89	64.5	1045	21	640	5,000,000
HFRT010	547	3.47	-2.67	63.6	1094	21	640	1,000,000
HFRT011	578	6.23	-4.45	80.5	996	21	640	10,000,000
HFRT012	552	5.34	1.78	80.5	979	21	640	5,000,000
HFRT013	560	5.78	-4.45	81.8	1099	21	640	1,000,000
HFRT014	552	2.67	-1.33	63.6	1059	21	640	10,000,000
HFRT015	543	8.01	1.33	64.1	1032	21	640	5,000,000
HFRT016	569	5.78	-2.67	63.2	1143	21	640	1,000,000
HFHT001	543	4.89	0.89	80.5	1246	538	620	10,000,000
HFHT002	534	4.89	0.44	81.8	1072	538	620	5,000,000
HFHT003	560	6.67	3.56	80.5	1112	538	620	1,000,000
HFHT004	601	4.45	4.00	81.4	952	538	620	10,000,000
HFHT005	538	4.00	2.67	82.3	1192	538	620	5,000,000
HFHT006	520	5.78	-1.33	83.6	1241	538	620	1,000,000
HFHT007	601	5.78	0.89	81.4	1170	649	650	10,000,000
HFHT008	529	4.00	-1.33	81.8	1179	649	650	5,000,000
HFHT009	574	4.89	-3.11	81.8	1241	649	650	1,000,000
HFHT010	556	4.89	0.44	80.5	1099	649	650	10,000,000
HFHT011	592	3.56	3.11	81.4	1263	649	650	5,000,000
HFHT012	534	4.00	-3.11	81.0	1072	649	650	1,000,000
HFHT014	534	6.23	3.56	100.1	1246	649	650	5,000,000
HFHT015	565	12.5	1.33	99.2	1134	649	650	1,000,000
HFHT016	560	7.12	-5.78	99.2	1192	649	650	10,000,000
HFHT018	560	7.56	1.78	98.3	1259	649	650	5,000,000
HFHT019	534	3.56	-1.78	63.6	1081	649	650	10,000,000
HFHT020	547	3.11	-0.44	63.6	1303	649	650	5,000,000
HFHT021	565	4.00	2.22	64.1	1165	649	650	1,000,000
HFHT022	596	3.56	-3.56	62.7	1103	649	650	10,000,000
HFHT023	560	2.67	1.78	63.2	1165	649	650	5,000,000
HFHT024	578	2.67	-4.00	63.2	1076	649	650	1,000,000
HFHT025	592	4.89	-5.34	99.2	1041	649	650	1,000,000
HFHT026	565	4.00	-6.67	99.2	1223	649	650	10,000,000

6 Experimental Loads

The designed test program outlined in Table 3 was performed. Processing of the raw data as obtained in-situ from the data acquisition system for each experiment allows for the determination of the normal load, P, tangential load, Q, and specimen clamping load, L_C, values. These values as obtained for the room-temperature and elevated temperature experiments can be seen in Table 4.

Specimen surface profiles were performed before and after each experiment to survey the consistency of specimen surface roughnesses before testing and document wear profiles observed post-test. From the pre-test surface profilometry, the average specimen surface roughness for HFHT and HFRT specimens was found to be Ra = 0.208 μm with a standard deviation of 0.074 μm. The fretting wear patch was also investigated using scanning electron microscopy. SEM micrographs of the post fretted surfaces for tested specimens were also catalogued for later analysis.

7 Damage Assessment

Due to the absence of a crack propagating bulk stress, a suitable damage inspection method must be employed to ascertain if a fretting crack has nucleated.

7.1 Crack Identification

The small, circular wear scar inherent to the spherical contact localizes the area in which cracks can nucleate. However, the micro-welds and wear debris of the fretting scar itself could potentially cover a nucleated crack opening. To address this, wear scars like those in the previous figures were first subjected to a smooth swab with ethanol to remove as much wear debris as possible before observation of the scars were investigated in a scanning electron microscope.

After removal of the wear debris, the contact wear patches were investigated in the SEM to identify nucleated or propagated fretting crack locations and orientations. Fretting cracks were found on both room temperature and elevated temperature tests and were found to propagate both crystallographically and noncrystallographically. Figure 14 illustrates a crystallographic fretting crack initiated at room temperature as observed from the specimen surface, and Figure 15 illustrates a noncrystallographic fretting induced crack obtained under

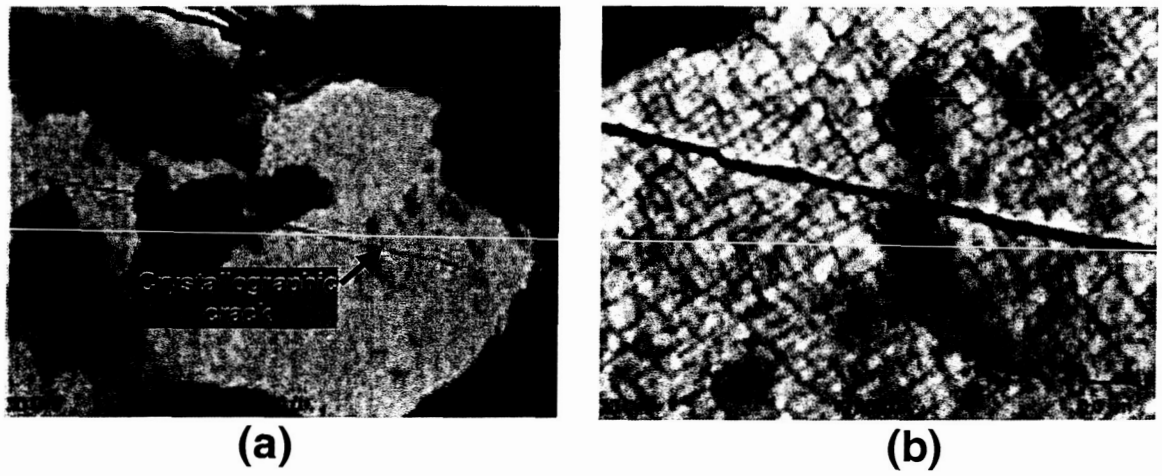

Fig. 14. Scanning electron micrographs showing fretting induced crystallographic cracking at the lower wear scar on the surface of room temperature (21°C) test specimen J3-30D-04. (a) A macro-view micrograph showing a crystallographic surface crack within the slip annulus. (b) A close-up micrograph of the crystallographic cracking in (a) highlighting crystallographic cracking across the microstructure.

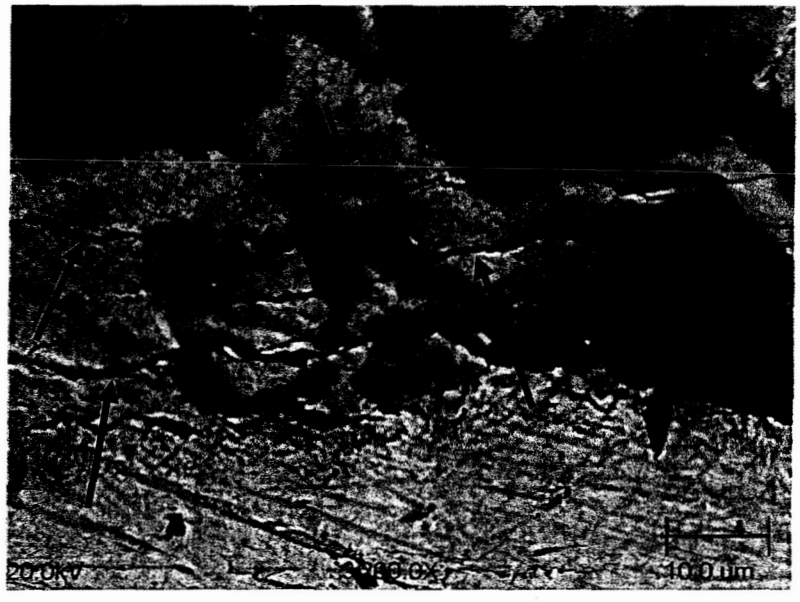

Fig. 15. Scanning electron micrograph showing fretting induced noncrystallographic cracking on the stick slip interface of the center wear patch on the surface of room temperature (21°C) test specimen J3-30D-02. Arrows identify cracks.

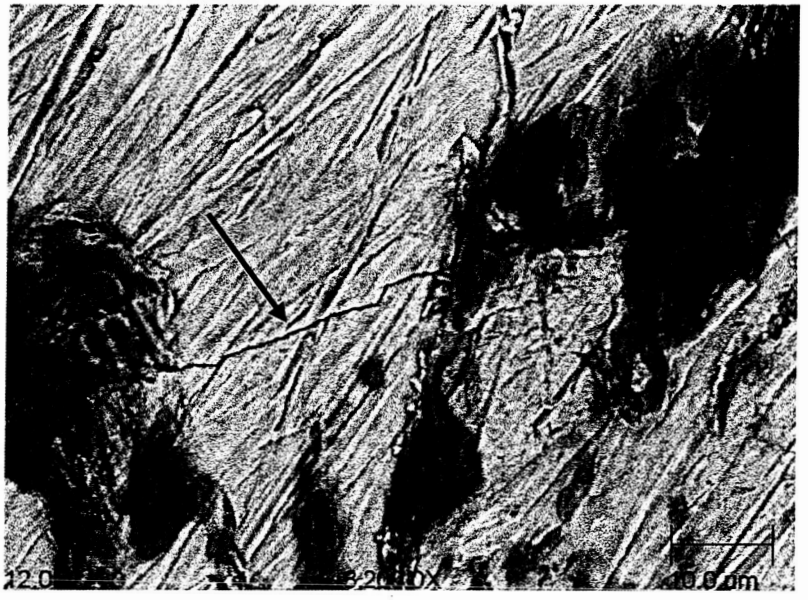

Fig. 16. Scanning electron micrograph showing a fretting induced crack in the slip annulus of the lower wear patch for elevated temperature (538°C) test specimen J3-30D-05. Arrow identifies crack.

fretting loads at room temperature. Figure 16 shows cracking as observed from a high-temperature test specimen. It is important to note that the high temperature operation caused significant oxidation of the specimen surface inhibiting view of the material microstructure. As a result, no comment can be made about the orientation of the crack with respect to the crystal orientation unless the orientation can be determined through alternate methods.

The location and orientation of the cracks as observed from the surface were then catalogued and recorded (see Table 5) according to the coordinate system in Figure 17. Note that Ω is the angular location of the cracking observed as measured from the x'-axis (positive clockwise as in Figure 17b), and Ω_c is the measured angle of crack orientation also measured from the x'-axis (positive clockwise as in Figure 17c). From these results it can be observed that the majority of observed cracking behavior was crystallographic for room temperature tests. Also note that significantly more cracking was observed in specimens oriented at $\Theta = \pm 30^o$. It is also important to note that significant oxidation of specimen surfaces during high temperature testing prevented determination of material axis orientations. As a result, cracks observed in the high temperature tests could not be classified as crystallographic.

7.2 Fracture Surface Investigation

Some of the specimens for which a nucleated crack was observed, a precision saw was used to remove material behind the wear scar and holes were drilled in the specimen in strategic spots around the wear scar to locate a stress concentration near the crack position. Care was taken to ensure that the cut plane was in the same orientation as the target crack. After fixing the specimen for application of an impact loading, a pendulum was swung to impose an impact bending load on the specimen and force fracture of the specimen at the identified crack location. The fracture surface was then surveyed in the SEM to further investigate the nature of the nucleated fretting cracks. Previous research has shown some success at identifying fretting crack initiation regions [15] by looking at the fracture surface. A series of SEM micrographs illustrating a representative fracture test result can be seen in Figures 18, 19, 20, ??, 21,and 22. The triangular facets observed in Figure 22 show evidence of crack propagation along a $\{111\}$ plane under only fretting load conditions. Observed crack depths were on the order of 25 μm.

Table 5
Post-test observations of crack locations and orientations for performed high-frequency fretting tests.

Test ID.	Spec ID.	Crack Group	Crack Type	Location Ω (deg)	Orientation Ω_c(deg)
HFRT005	J3-30D-01	1	crystallographic	0	-79
	J3-30D-02	1	noncrystallographic	0	arc along ID
		2	crystallographic	90	80
		3	crystallographic	180	77 to 83
HFRT006	J3-30D-01	1	noncrystallographic	45	arc along ID
		2	noncrystallographic	135	arc along ID
	J3-30D-02	1	crystallographic	-105	-8 to -15
		2	noncrystallographic	0	arc along ID
		3	crystallographic	90	-8
		4	crystallographic	180	84 to 85
HFRT007	J3-30D-01	1	crystallographic	180	-78 to -80
	J3-30D-02	1	crystallographic	-90	-9 to -12
HFRT008	J3-30D-03	1	crystallographic	180	75
	J3-30D-04	1	crystallographic	-90	145
		2	crystallographic	90	8
HFRT009	J3-30D-03	1	crystallographic	0	73 to 75
		2	crystallographic	180	83
	J3-30D-04	1	crystallographic	-90	4
		2	noncrystallographic	-45	arc along ID
		3	crystallographic	0	96 to 99
		4	crystallographic	180	102 to 103
HFRT011	J3-001-05	1	noncrystallographic	15	
	J3-001-06	1	crystallographic	135	45
		2	crystallographic	-135	130
HFRT012	J3-001-05	1	crystallographic	-60	56
	J3-001-06	1	noncrystallographic	0	arc along ID
		2	crystallographic	-135	132
HFRT013	J3-001-06	1	crystallographic	30	135
		2	crystallographic	-135	128
HFHT005	J3-30D-05	1	?	-45	70
		2	?	0	79
		3	?	0	97
		4	?	30	104
		5	?	180	

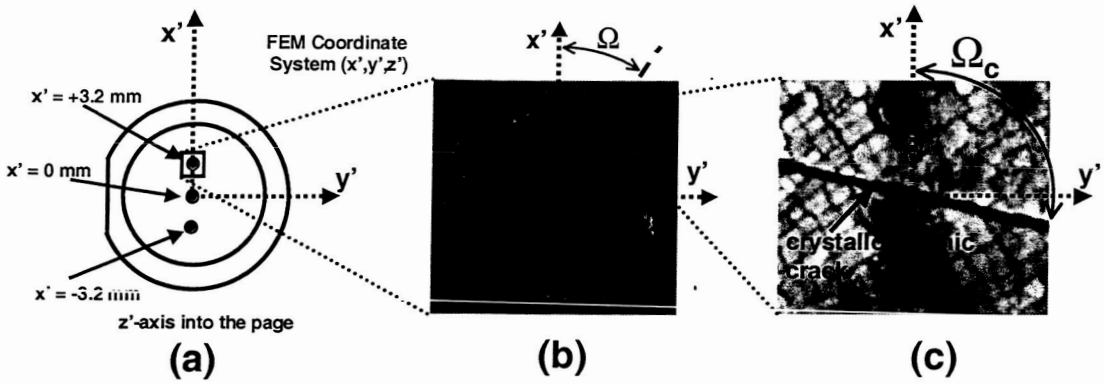

Fig. 17. Schematic highlighting the crack location and orientation coordinate systems and notation. (a) Schematic of the specimen and contact locations with respect to the FEM coordinate system. (b) Schematic defining the crack angular location, Ω, about the slip annulus. (c) Schematic defining the crack orientation angle, Ω_c.

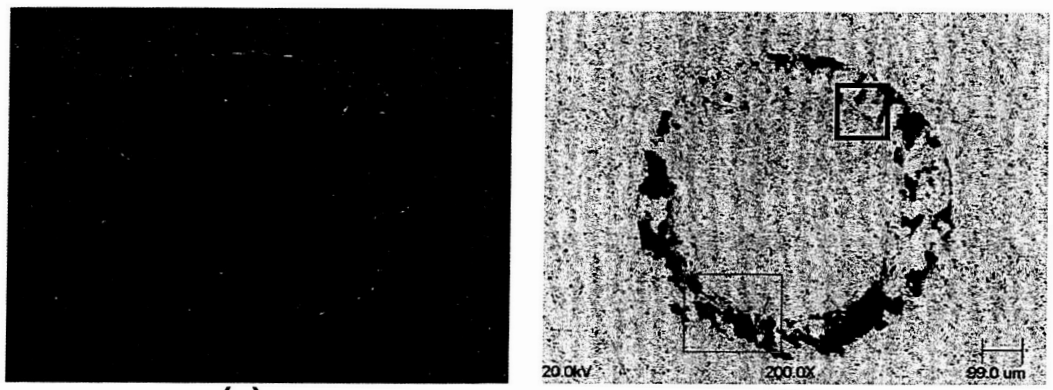

Fig. 18. SEM micrographs showing (a) a secondary electron, and (b) backscattered electron image of the upper wear patch of specimen J3-001-06. The black box highlights the target crack for break-open testing.

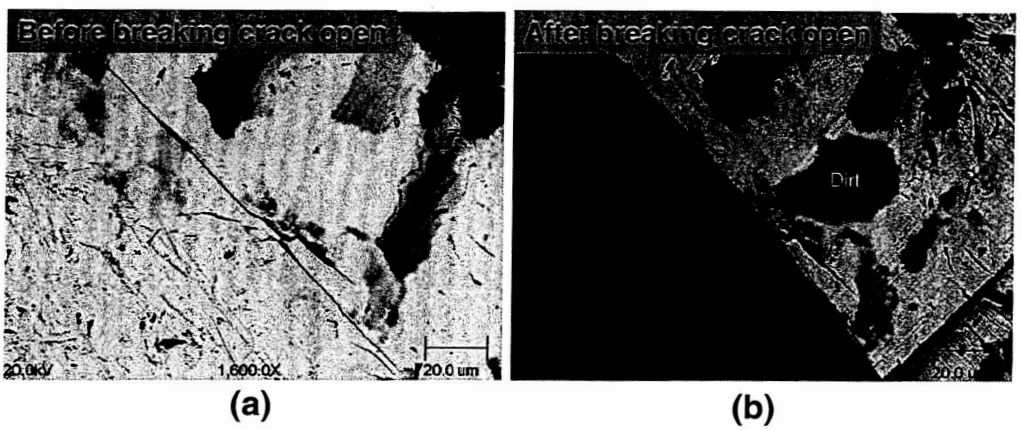

Fig. 19. Backscatter micrograph of the target crack on specimen J3-001-06 (a) before, and (b) after breaking the crack open.

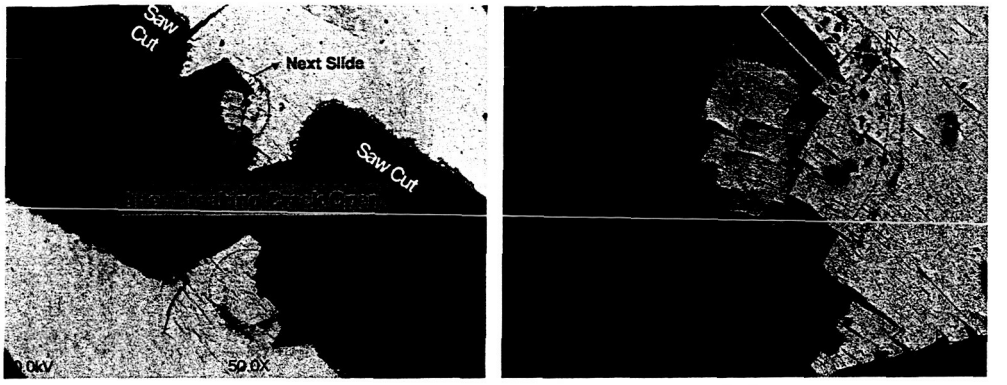

Fig. 20. Post-fracture SEM micrographs (a) highlighting the saw cuts used to locate a stress concentration near the desired wear scar, and (b) a close-up micrograph higlighting the location of the target crack. The location of the pre-fracture wear scar on specimen J3-001-06 is indicated by the dashed line circles.

Fig. 21. Close-up SEM image of the targeted fretting crack face of specimen (J3-001-06). Arrows only indicate crack growth away from the disk surface and into the specimen material and does not imply the exact crack growth path is known. Note that the extent of the fretting crack is identified by the disk surface and the fracture surface identified as the lab overstress region.

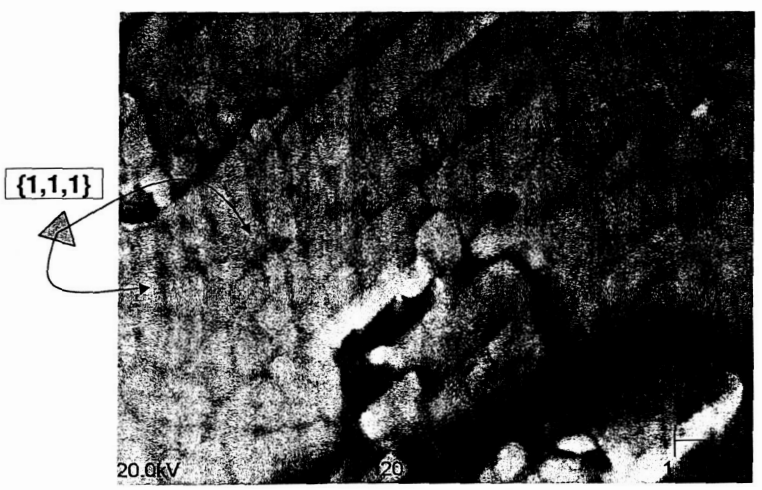

Fig. 22. SEM micrograph of the microstructure of a targeted fretting crack face showing triangular facets characteristic of crack propagation along {1 1 1} octahedral planes of FCC single crystals.

8 Conclusions

A high-frequency, high-temperature fretting fatigue load frame capable of in-situ monitoring of critical fretting contact parameters for a dissimilar, anisotropic contact has been constructed. Running a room temperature (21°C) and elevated temperature (538°C and 649°C) test program with the designed rig resulted in the following conclusions and observations:

- Piezoelectric stacks can be successfully used to apply well-controlled fretting loads at frequencies greater than 600Hz.
- Fretting contact stresses alone with no applied specimen bulk stress can nucleate and propagate cracks in single crystal nickel materials.
- Both crystallographic and non-crystallographic cracking was observed in tests performed at room temperature.
- Crystallographic cracks were observed to nucleate and subsequently propagate along {1 1 1} octahedral planes under fretting loads.
- Material orientation of single crystal nickel materials has a significant effect on the fretting crack behavior and damage.
- Fretting induced surface cracking can be identified through the use of scanning electron microscopy.
- With an appropriately machined specimen, an impact fracture rig can be successfully employed to break open and expose small cracks induced by fretting contact.

References

[1] D. W. Hoeppner, Mechanisms of fretting-fatigue and their impact on test methods development, in: M. H. Attia, R. B. Waterhouse (Eds.), Standardization of Fretting Fatigue: Test Methods and Equipment, ASTM STP 1159, American Society of Testing and Materials, Philadelphia, PA, 1992, pp. 23–32.

[2] D. A. Hills, A. Mugadu, An overview of progress in the study of fretting fatigue, Journal of Strain Analysis for Engineering Design 37 (6) (2002) 591–601.

[3] T. N. Farris, H. Murthy, J. F. Matlik, Fretting fatigue, in: R. O. Ritchie, Y. Murakami (Eds.), Comprehensive Structural Integrity: Fracture of Materials from Nano to Macro, Vol. 4, Elsevier Science, 2003.

[4] R. B. Waterhouse, Fretting fatigue, International Materials Reviews 37 (1992) 77–96.

[5] M. P. Szolwinski, T. N. Farris, Mechanics of fretting fatigue crack formation, Wear 198 (1996) 193–107.

[6] D. A. Hills, D. Nowell, Mechanics of Fretting Fatigue, Kluwer Academic Publishers, Netherlands, 1994.

[7] J. F. Matlik, T. N. Farris, High-frequency fretting fatigue experiments, in: Y. Mutoh, S. E. Kinyon, D. W. Hoeppner (Eds.), Fretting Fatigue: Advances in the Basic Understanding and Applications, ASTM STP 1425, American Society of Testing and Materials, West Conshohocken, PA, 2003, pp. 251–272.

[8] D. A. Hills, D. Nowell, The development of a fretting fatigue experiment with well-defined characteristics, in: M. H. Attia, R. B. Waterhouse (Eds.), Standardization of Fretting Fatigue: Test Methods and Equipment, ASTM STP 1159, American Society of Testing and Materials, Philadelphia, PA, 1992, pp. 69–84.

[9] H. Murthy, P. Rajeev, M. Okane, T. N. Farris, Development of test methods for high temperature fretting of turbine materials subjected to engine-type loading, in: Y. Mutoh, S. E. Kinyon, D. W. Hoeppner (Eds.), Fretting Fatigue: Advances in the Basic Understanding and Applications, ASTM STP 1425, American Society of Testing and Materials, West Conshohocken, PA, 2003, pp. 273–288.

[10] R. Bramhall, Studies in fretting fatigue, Ph.D. thesis, Oxford University (1973).

[11] J. J. O'Connor, The role of elastic stress analysis in the interpretation of fretting fatigue failures, in: R. B. Waterhouse (Ed.), Fretting Fatigue, Applied Science Publishers, London, 1981, Ch. 2, pp. 23–66.

[12] S. Fouvry, P. Kapsa, L. Vincent, A multiaxial fatigue analysis of fretting contact taking into account the size effect, in: D. W. Hoeppner, V. Chandrasekaran, C. B. Elliott (Eds.), Fretting Fatigue: Current Technology and Practices, ASTM STP 1367, American Society of Testing and Materials, West Conshohocken, PA, 2000, pp. 167–182.

[13] H. Murthy, G. Harish, T. N. Farris, Efficient modeling of fretting of blade/disk contacts including load history effects, Journal of Tribology (2004) in press.

[14] D. DeLuca, C. Annis, Fatigue in single crystal nickel superalloys, Office of Naval Research, Department of the Navy FR-23800.

[15] T. N. Farris, H. Murthy, D. B. Garcia, J. F. Matlik, Fretting fatigue of single crystal/polycrystalline nickel subjected to blade/disk contact loading, in: Proceedings of the World Space Congress, Vol. IAC-02I.1.08, Houston, TX, USA, 2002.